Exp Fluids (2009) 47:509–526
DOI 10.1007/s00348-009-0682-x

RESEARCH ARTICLE

Evaluation of the performance of high-speed PIV compared to standard PIV in a turbulent jet

M. Falchi · G. P. Romano

Received: 20 December 2007 / Revised: 21 February 2009 / Accepted: 3 May 2009 / Published online: 24 May 2009

Abstract In this paper, a comparison between two particle image velocimetry (PIV) systems, one based on a standard cross-correlation charge coupled device (CCD) camera with pulsed laser and another using high-speed complementary metal oxide semiconductor (CMOS) camera with continuous laser is performed. The objective of the paper is to point out advantages and disadvantages of the two systems when computing large and small flow scale statistics. The comparison is performed on velocity measurements in the near and far fields of a circular water jet: on this flow several experimental data and empirical self-similarity laws are available for comparisons. The results show that both systems are suitable for measurements with a preference for the standard one when investigating small-scale statistics. This result depends on the lower number of effectively independent samples acquired by a high-speed system and on the higher noise levels of CMOS sensors in comparison to CCDs.

1 Introduction

The measurement of velocity fields with high spatial and temporal resolutions is a fundamental task for experimental and theoretical fluid-mechanics. Since the beginning of its development, particle image velocimetry (PIV) has allowed velocity recording at high spatial resolutions, in the order of 5×10^3 m^{-1}, with standard cameras (Westerweel et al. 1997; Scarano 2003); on the other hand, only recently high temporal resolutions similar to other velocity measuring techniques such as laser doppler anemometry (LDA), in the order of 10^3 Hz, have been obtained by using high-speed cameras (Raffel et al. 1995; Brucker 1997; Lecordier and Trinité 1999; Etoh et al. 2001). The diffusion of such high-speed cameras at relatively moderate costs mainly depends on changes in the architecture of the sensor and in the different ways in which information are acquired and transferred from camera sensor elements to the memory.

Basically, sensor elements used in standard PIV cameras, usually known as cross-correlation cameras, are based on charge coupled device (CCD) architecture, i.e. on a solid-state chip in which pixels are charged by incoming photons, transferred through a very limited number of output nodes, often one, to be converted to voltage, buffered, and sent off-chip as analogue signals. All of the pixels can be devoted to light capture resulting high output uniformity which is the ratio between average illumination level and the difference between the brightest and darkest levels, and represents the response of the different pixels of the sensor under the same illumination conditions. On the other hand, sensors for recent advanced high-resolution high-speed cameras are based on complementary metal oxide semiconductor (CMOS), i.e. on semiconductor technology in which each pixel has its own charge-to-voltage conversion, and the sensor often also includes digitization circuits, so that the chip outputs digital bits. To overcome the low light pixel sensitivity in CMOS sensors, due to reduced fill factor, a large pixel size is used, about 20 μm for CMOSs and 5–7 μm for CCDs. This is equivalent to higher sensitivity to low illumination levels. Other advantages are the low power supply and power dissipation, which allows the close spacing of many sensors. The related major disadvantages derive from high sensitivity to

M. Falchi · G. P. Romano (✉)
Department of Mechanics and Aeronautics,
University "La Sapienza", Via Eudossiana n° 18,
00184 Rome, Italy
e-mail: romano@dma.ing.uniroma1.it

noise, low magnification factor and high number of "dark elements", i.e. elements not responding to light intensity variations, due to cost reduction in production system. These disadvantages are usually reported as possible drawbacks to be considered when performing detailed investigations on turbulence by using PIV systems based on high-speed CMOS cameras (also known as high-speed or time resolved PIV) (Hain and Kahler 2005). Recent comparative investigations among CMOS cameras revealed that not all of them have same performances in comparison with CCD ones (Hain et al. 2007). In particular, it has been shown that it is extremely problematic in terms of noise levels to use high-speed CMOS cameras with image intensifiers. On the other hand, when recent CMOS cameras are used, almost the same signal to noise ratio (SNR) and spatial uniformity as CCDs is attained. This is true if the illumination levels are not too low in which case, departures from the linear relation between incoming illuminance and outcoming signal take place. Thus, the illumination level is a crucial point when using high-speed PIV based on CMOS cameras. In this sense, it is correct to speak about performances of the whole high-speed system rather than of the camera alone.

It is particularly important to clarify if an high-speed system is able to reproduce results similar to standard PIV, especially when considering the widespread use of high-speed PIV in investigating many different flow fields from bio-mechanics (Triep et al. 2005), to engine mechanics (Towers and Towers 2004), bluff body wakes (Williams et al. 2003) and shock wave dynamics (Raffel et al. 1995; Burgmann et al. 2006). Nowadays, in almost all industrial and basic research applications, the interest is not simply focussed on mean fields, which are more or less independent of the specific illumination and acquisition system or image analysis algorithm, but especially on higher order statistics including velocity derivatives and kinetic energy dissipation. These quantities are much more dependent on noise sources than first-order statistics and are required to calibrate proper numerical simulation codes.

In the present paper, combined use of conventional and high-speed PIV is adopted to point out the differences on velocity and velocity derivative statistics on an axi-symmetric turbulent water jet whose Reynolds number, based on jet diameter D, is equal to about 2×10^4. The circular jet flow has been selected because it is well known in terms of the evolution along the streamwise and transverse directions, i.e. self-similar solutions, so that a strict comparison with several available data sets and empirical theories is possible. The aim of the paper is to establish if noise and other disturbances could give incorrect statistical evaluations, especially of higher order statistics, when using high-speed in comparison to conventional PIV.

As previously stated, in performing such a comparison, the whole PIV system has to be considered. In theory, not only the camera, but also the illumination source, the optics and the seeding must be optimised separately for each image acquisition system (high-speed and standard cross-correlation PIV). On the other hand, for a proper comparison, image analysis, pre-processing and processing, have to be performed similarly. To this end, the image analysis algorithm applied on the images acquired by the two systems is exactly the same. Same software, DaVis from La-Vision, with same analysis parameters have been used. Also, the statistical analysis on velocity data is performed similarly with the same algorithms and number of total images for statistics, 10,000 samples (statistical dependence or independence between samples will be also considered). In practice, the differences between the two set-ups are limited to the illumination system, 7 W continuous Ar-ion laser for high-speed PIV and 120 mJ pulsed Nd–Yag laser for standard PIV, and to the camera for image acquisition, CCD $1{,}376 \times 1{,}040$ elements for standard PIV, CMOS $1{,}024 \times 1{,}024$ elements working at 2 kHz for high-speed PIV, while optics and seeding remain more or less the same.

2 Experimental systems

The water jet apparatus is detailed in Fig. 1; the facility consisted of an axisymmetric water jet flowing downstream through a 50:1 area contraction nozzle placed at the end of a pipe. The Reynolds number based on average jet outlet velocity, U_o, and the jet diameter $D = 2$ cm was $Re \approx 20{,}000$; the Reynolds number based on the Taylor microscale, $R_\lambda = \lambda u'/\nu$, where λ is the Taylor microscale, u' is the rms velocity and ν the kinematic viscosity, was about 150, evaluated in the jet far field. For the reference system, x and y were, respectively, the distance along the jet axis and along the vertical direction, with origin on the jet axis at the nozzle. Downstream of the nozzle the flow entered into a tank with height and width $\approx 30D$, length $\approx 60D$. The measurements were taken in this tank close to the nozzle from $2D$ to about $10D$, the near jet region, and far from the nozzle from about $25D$ to $30D$, the far jet region. Due to the limited size of the tank, the jet had to be considered as confined rather than free. This choice reflected the fact that in practical applications and in numerical simulations the jet is usually confined. All the contractions, pipe and tank were made by transparent Perspex to allow full optical access allowing video-cameras to be placed anywhere around the tank. Previous measurements confirmed that the flow field was unaffected by pump external forcing frequencies and that it was axially symmetric without swirl (Romano 1998).

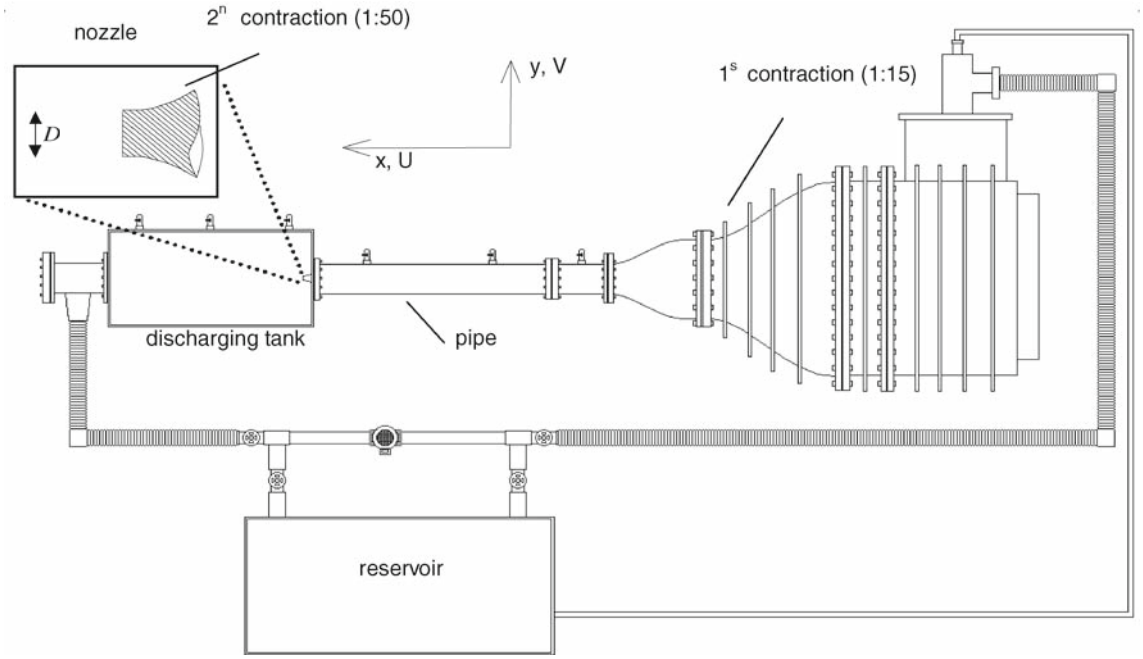

Fig. 1 Experimental set-up and co-ordinate system

The cross-correlation and high-speed systems are described separately. The standard cross-correlation system consisted of a LaVision 2C PIV system. The illumination was provided by a double Nd–Yag laser, 532 nm wavelength, with maximum 120 mJ per pulse, 7 ns pulse duration. Image acquisition was performed using a cross-correlation, 12-bit BW, PCO CCD camera with 1,376 × 1,040 pixel resolution imaging a region as large as 8*D*, with a resulting spatial resolution equal to 10^4 m^{-1} in the near jet region.

In the far jet region the imaged area was reduced to 4*D*, 2×10^4 m^{-1} for the spatial resolution. For both cases the repetition rate of the system was 10 Hz, the maximum time resolution of the system. The time delay between the two images was optimised to 1 ms and 80 mJ per pulse were effectively used. The light incoming at each pixel was averaged over 7.9 × 7.9 μm sensor size. The magnification factor was 95 pixel/cm (the imaging magnification, i.e., chip size/imaged size, was equal to 0.076) and the used camera objective was a Nikon F 50 mm focal length with aperture equal to 1.8.

The high-speed system consisted of a high-speed 8-bit BW, Photron APX CMOS camera with 1,024 × 1,024 pixels resolution, imaging a region as large as 6*D*, with a spatial resolution equal to the previous one, i.e. about 10^4 m^{-1} in the near jet region and 2×10^4 m^{-1} in the far region. The light incoming at each pixel was averaged over 17 × 17 μm sensor area. The magnification factor was 94 pixel/cm (the imaging magnification was equal to 0.15) and the camera objective was the same as before. The camera was able to acquire 2,000 images per second at full spatial resolution, even if for the present measurements, the data were under-sampled at 1 kHz. The illumination was provided by a continuous Ar-ion laser, 488–514 nm in wavelength, with a maximum power equal to 7 W. Considering the used shutter time, 1/2,000 s, the effective energy at disposal to the camera sensor was about 4 mJ, i.e., much less than for the cross-correlation camera; however, by considering the different sensor size, the amount of light reaching each pixel for the high-speed system was only four times lower than for the standard system. It is important to notice that these limiting values for the energy reaching the high-speed sensor are similar to those available when using high-repetition rate pulsed lasers.

Calibrated hollow glass spheres, diameter 10 μm, were used as seeding particles. Theoretically, due to the lower illumination provided by the continuous laser, the high-speed system would have required larger particles in comparison to the standard one. However, this would have reduced the respond to turbulent fluctuations due to the well known low-pass effect in which the cut-off frequency roughly decreases as the inverse of the particle size squared as highlighted by Hinze (1975). Thus, we preferred not to include the particle size as a possible source of variation when considering the ability to perform turbulence measurements by the two PIV systems. Seeding was introduced both upstream of the 50:1 contraction and within the tank so that tracers were present both in the jet and in the ambient fluids.

For both systems, the instantaneous vector fields were derived from an advanced image deformation multi-pass PIV cross-correlation algorithm with window offset, adaptive window deformation and Gaussian sub-pixel approximation, DaVis by LaVision Gmbh. In view of the applicability of the present results to other experimental conditions, we preferred to use reliable and simultaneously commercial PIV software. A detailed description of the features and performance of the algorithm is given in Stanislas et al. (2008). In particular, the previous paper reports the evaluation of mean bias and rms errors, which are of course dependent on the kind of flow and on the image quality. Roughly speaking, for the DaVis software the mean bias error is evaluated as less than 0.5%, while the rms error is around 5%, i.e. about 0.04 pixel. These values have been derived by performing PIV analysis on artificial images after comparison with the reference known solution. The window size was 32 × 32 pixels, with 75% overlapping, thus the spacing between velocity vectors was 8 pixel corresponding to about 1 mm with an effective velocity resolution in space of 10^3 m^{-1}. This spacing was about ten times larger than the Kolmogorov length scale, $\eta = 0.08$ mm, and about equal to one Taylor microscale.

The flow scales were obtained with the standard laws reported by Tennekes and Lumley (1970), by using the hypothesis of homogeneous and isotropic flow. In particular, Taylor and Kolmogorov scales are computed by using the isotropic form of turbulent kinetic energy dissipation (Eq. 4 in the following).

In Table 1, the flow scales evaluated with the two systems are summarised. The values are basically the same, except for the integral scale for which the maximum deviation between computed scales is less than 20%, the error on this evaluation is about 0.1 mm, i.e. 1.5%. The integral scale was evaluated as the separation at which the spatial correlation coefficient attains the value $1/e$, thus the observed difference reflected an effective major contribution of small correlated scales in data from high-speed system in comparison to data from the standard one and this is confirmed by the slightly larger value obtained for the Taylor microscale.

The complete acquisition set for each system consisted of 10,000 images pairs which were used to evaluate average velocity fields and other turbulent statistical quantities, i.e. rms values, Reynolds stresses, skewness and flatness factors, mean square velocity derivatives, turbulent kinetic energy dissipation.

Table 1 Flow scales obtained from standard and high-speed PIV systems

	Integral length scale L (mm)	Taylor microscale λ (mm)	Kolmogorov scale η (mm)
Cross-correlation	7.2	1.03	0.081
High-speed	5.9	1.08	0.079

To assess the quality of the present PIV data in comparison to previous studies, the following available data sets or empirical laws were used:

- Hot wire (HWA) data from Antonia and Burattini (2004) obtained in a circular air jet at $Re = 47{,}000$;
- Laser doppler anemometry (LDA) data from Djeridane et al. (1993) obtained in a circular air jet at $Re = 20{,}000$;
- The following empirical laws obtained from self-similarity arguments by Hussein et al. (1994), given in Eq. 1, and by Kuang et al. (2001), in Eqs. 2 and 3.

$$\frac{U}{U_o} = e^{-(Y^2/2)} \tag{1}$$

$$\frac{U}{U_o} = \mathrm{sech}^2\left(\frac{Y}{2\beta}\right) \tag{2}$$

$$\frac{\overline{uv}}{U_o^2} = \beta \tanh\left(\frac{Y}{2\beta}\right)\mathrm{sech}^2\left(\frac{Y}{2\beta}\right) \tag{3}$$

where capital letters are used for mean values, lower case is used for fluctuating quantities, $Y = y/y_o$ with y_o being the vertical distance for which $U = U_o/2$ and β is an empirical constant equal to 1.8 for the present data.

3 Image quality analysis

Firstly, an image quality analysis has been performed. Images were background pre-processed by subtracting the minimum intensity at each pixel as evaluated over the entire set. In Fig. 2, examples of such images from the two PIV systems after background pre-processing are given. Some light extinction from the bottom to the top of the images can be noticed, light is coming from the bottom, even if the use of a reflecting mirror at the top greatly reduced the problem. In any case, both images given in Fig. 2 are of good quality with good contrast and without saturation. The image from the standard system shows a higher scattered light intensity, especially within the jet, in comparison to the high-speed one. The maximum intensity level is about four times that attained in the high-speed image in agreement with previously reported expectations from the different illumination sources.

From the enlargements given at the bottom of Fig. 2, it can be noticed that while the appearance of sub-windows in the region outside of the jet were similar, there were noticeable differences for sub-windows within the jet core. It is important to establish if these differences in illumination could alter PIV performance. Thus, the signal to

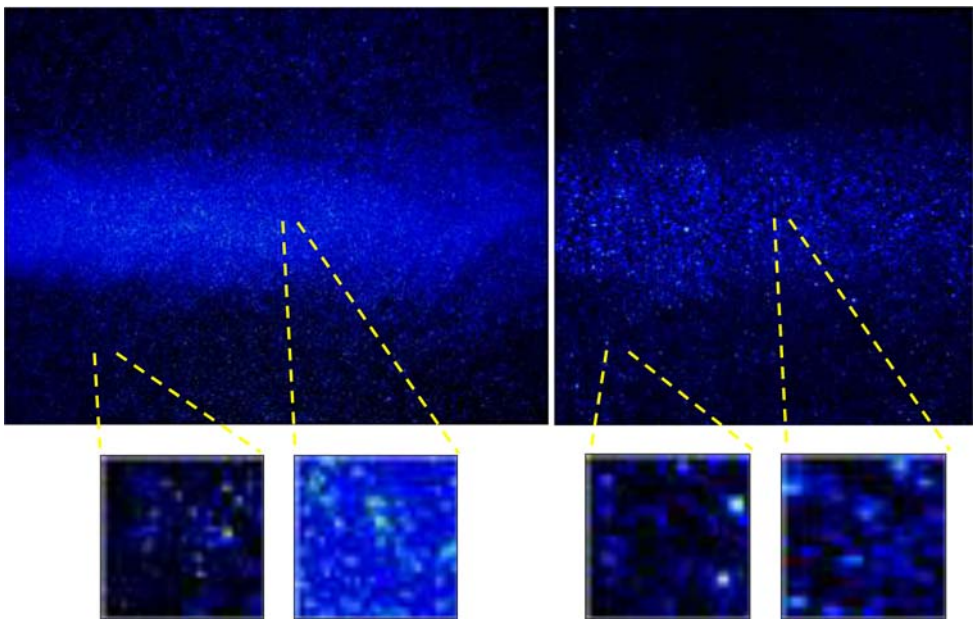

Fig. 2 False colours examples of images acquired by the standard PIV system (on the *left*) and by high-speed one (on the *right*). Flow direction from left to right. At the bottom, details of a 32 × 32 pixel window outside the main jet, for each couple on the left, and at the centreline, for each couple on the right

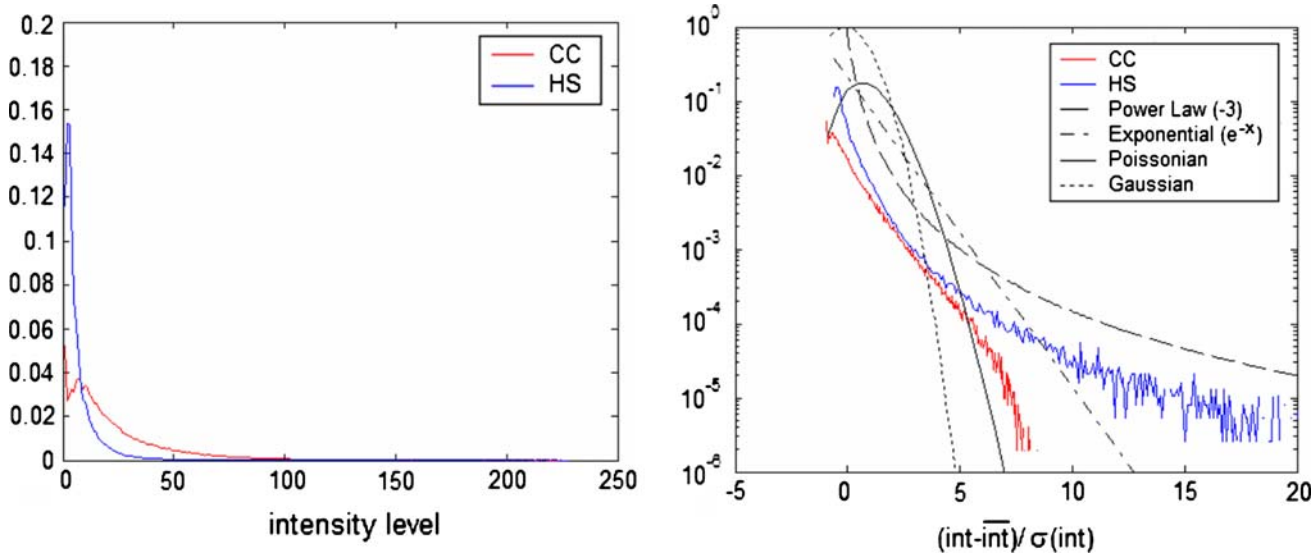

Fig. 3 Averaged normalised probability density functions of the *grey* light intensity at each pixel for the standard (CC in *red*) and high-speed (HS in *blue*) PIV systems. Linear plot of intensity levels, on the *left*, and logarithmic plot of normalised intensity levels, on the *right*

noise ratio, SNR, was evaluated by considering in each image the average intensity level in regions with seeding particles and by dividing it using the average level in regions without particles. Similar results were attained by the two systems, i.e. SNR = 10 for images coming from the standard system and SNR = 7 for the high-speed one, so that similar performance could be expected. These results were in agreement with those reported by Hain et al. (2007). The values obtained for SNR also ensured to be in the linear working region for the sensors, Figs. 5 and 6 in the paper by Hain et al. (2007).

In Fig. 3, the normalised intensity levels PDFs, with integral equal to 1, are given for the images of Fig. 2 where intensity levels are reported as integers between 0 and 255 for both cameras (consider that the minimum intensity has been subtracted in pre-processing). On the left part, in linear scale, it is possible to note that the standard PIV system exhibits an average intensity, equal to 23, about four times higher than that of the high-speed one, equal to 6. Similarly, there is larger intensity variability for the standard PIV system in fact the standard deviation is a factor two higher than for the high-speed system, 24 and

11, respectively. This means that the images from standard PIV contain brighter and better contrasted particle images in comparison to the high-speed one. On the right part of Fig. 3, the PDFs are reported on a vertical logarithmic scale while in the horizontal axis, the mean intensity value is subtracted and the result is divided by the standard deviation of intensity. This plot clarifies that both distributions are far from Gaussian or Poissonian PDFs, also reported in the figure. It is quite clear that the standard system attains a much lower intensity level in comparison to the high-speed one (from about five standard deviations on). In particular, there is a longer tail towards high intensity levels for the high-speed system in comparison to the standard one. This tail is close to a power-law distribution with exponent −3. On the other hand, the tail in the standard system can be well approximated by an exponential behaviour e^{-x}. Such an exponential PDF indicates that there is almost independence among the different intensity levels in the standard PIV image, while the power-law behaviour points out a much stronger relation between levels for the high-speed system. From Fig. 2, this seems to depend on the different imaged tracer size which is larger for the high-speed system, thus providing an intensity level gradation among neighbour pixels, and most likely to a higher level of noise in the CMOS sensor. The last conclusion is confirmed by the fact that for intensity levels larger than five standard deviations over the mean the major contribution is due to residual background.

4 Convergence of statistical moments

It is important to describe in detail the acquisition procedures used to obtain the statistical ensemble. For the standard PIV system, the 10,000 sample ensemble results from 10 subsets of 1,000 images each one. From the repetition rate of 10 Hz, each acquisition took about 100 s, i.e. about 2×10^3 integral time scales, as derived from integral length scales measured from correlation functions in the far field, i.e. $l \approx 7$ mm, divided by the local mean velocity, about 0.25 m/s. Thus, the whole ensemble corresponds to about 2×10^4 integral time scales so that all samples are statistically independent. For the high-speed system, the same statistical ensemble is derived from 200 subsets of 50 images each one. Being the camera rate equal to 1 kHz, each subset took about 0.05 s, i.e. about two integral time scales. Thus, the acquisition of all subsets took about 4×10^2 integral time scales and the samples are not all statistically uncorrelated. This is something obvious by considering that high-speed PIV is used for dynamical investigations of flow fields, thus just acquiring time-correlated samples. In the present comparison, the attention was focussed on velocity statistics still retaining the basic characteristic of mostly correlated samples when a high-speed PIV system is employed. The choice of 200 subsets of 50 images was a compromise between the statistical and dynamical investigation constraints. In comparing the amount of data between the two systems, there is a factor about 30 between the effective number of independent samples acquired with standard and high-speed systems, in practice 10,000 samples acquired with the standard system correspond to about 400 samples acquired with the high-speed one. The previous aspects must be considered when comparing statistics obtained by the two systems, as also reported by Bendat and Piersol (1971).

To evaluate the effective differences in computing statistical moments from the two systems, tests on statistical convergence have been performed. In Fig. 4, the PDF of axial velocity obtained from the two systems with different samples number, 400, 2,000 and 10,000, at the centreline and in the shear layer are compared at $x/D = 5$. Both systems behave similarly and the approach to the limiting PDF seems to be similar at the two selected positions. It is also important to point out an almost vanishing, or at least strongly reduced, peak locking effect for both systems (especially when 10,000 samples are considered). Thus, even if samples acquired with the high-speed system are not entirely statistically uncorrelated the PDF distributions converge similarly to the standard PIV system. The selected number of samples for the present data acquisitions, 10,000, seems to be satisfactory to derive a quite smooth PDF. It is further evaluated the behaviour of the first four statistical moments as a function of the sample size.

In Fig. 5, the relative difference to the final value is shown for one point in the shear layer. The convergence of the moments is actually effective, except for the skewness factor, which is almost zero at these positions, thus presenting in the relative difference large oscillations for both systems. The convergence of data for the standard system is very good, differences are within ±10% already for $N > 1{,}500$. On the other hand, for the high-speed system it is necessary to acquire a number of samples $N > 7{,}000$ to attain a similar level.

This is partially due to the previously reported different number of effectively independent samples, but some effects of the different distribution of light intensity levels, i.e. the different SNR, as observed in previous section, Fig. 2, cannot be excluded especially on the higher moments. Nevertheless, the observed convergence of statistical moments is very satisfactory for both systems. It is important to point out that for other measurement positions in the jet core or in the shear layer the statistical convergence is similar. The acquired samples give an error not larger than ±2.5% up to the fourth-order moment. On the other hand, for points in the outer region this error can be as high as ±5%.

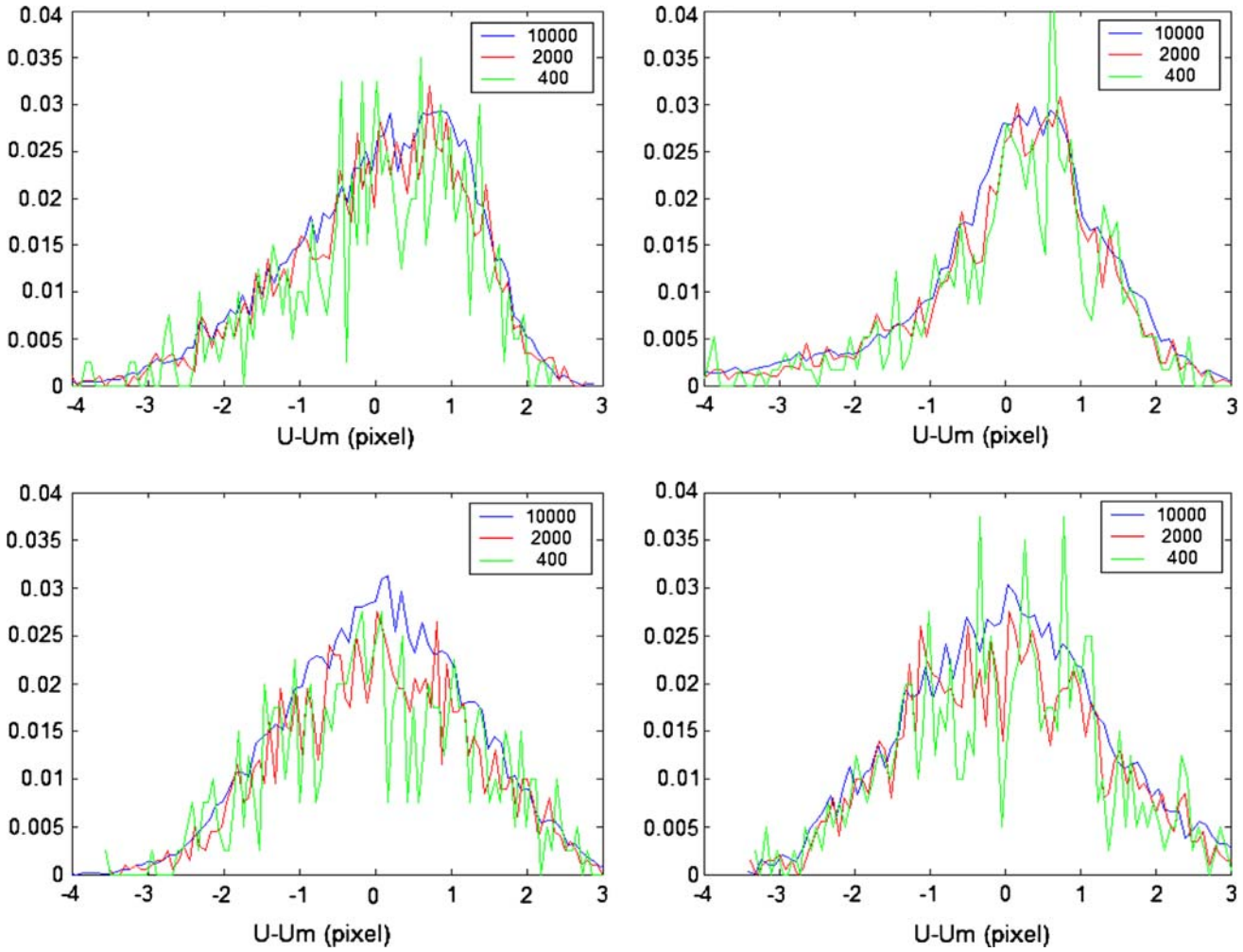

Fig. 4 Normalised probability density functions of the axial velocity component obtained with different sample number close to the jet centreline, at the top, and within the shear layer, at the bottom. Results from the standard PIV system (on the *left*) and for the high-speed one (on the *right*)

5 Results and comparisons

The results will be presented separately for statistics of velocity—average velocity, rms values, skewness and flatness factors—and of velocity derivatives—mean square values, kinetic energy dissipation.

5.1 Statistics of the velocity field

The average flow field behaviour for the axial velocity component, non-dimensional by the jet exit velocity, is reported in Fig. 6 for both PIV systems—jet flow from left to right. It is possible to observe that the derived fields are very similar. Consider that the region between $x/D = 7.5$ and $x/D = 9.5$ is not acquired by the high-speed camera due to the reduced camera sensor size along the horizontal. The velocity decreases when moving from the centreline along the vertical and more slowly along the horizontal. The jet core, i.e. the axial region in which the velocity is close to the jet exit velocity, is about 5–6 in diameter, thus in good agreement with Cohen and Wygnansky (1987), Liepmann and Gharib (1992), Antonia and Burattini (2004) and Burattini et al. (2005).

In Fig. 7, the rms axial velocity is represented. The overall behaviour of the two fields is similar, in fact the shear layers develop with the same turbulence intensities, i.e. maximum value equal to more than 15%. However significant differences are noticed, in particular there is a lower quality and more disturbances, in the form of more or less vertical bands, in the high-speed system results. The reason for this behaviour basically resides in the differences between the statistical ensemble used for the two PIV systems, as discussed in the previous section. Even if the shape of the PDFs and the convergence of moments are satisfactory, the sub-set duration for the high-speed system, does not allow deriving a smooth flow field. The reason for

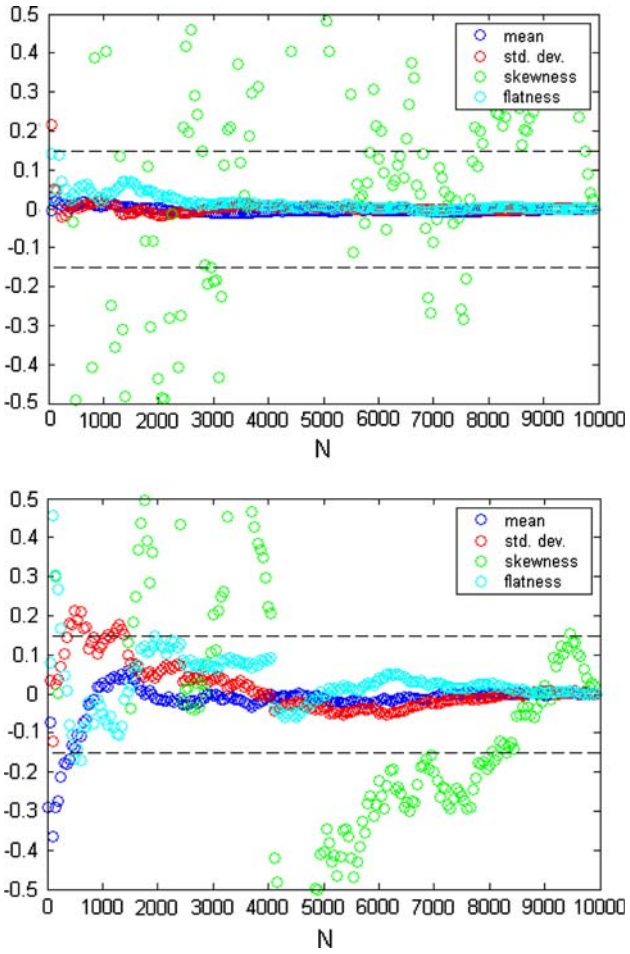

Fig. 5 Relative differences to final values for the first four statistical moments as a function of number of samples. Evaluation for standard (at the *top*) and high-speed (at the *bottom*) systems in the shear layer. The horizontal dashed lines indicate a difference of ±15%

this behaviour resides in the fact that during image acquisition of each subset the flow is moving downstream over about one jet diameter. Thus, traces of this "high-speed pattern movement" appears in the form of more or less vertical bands from one subset to the other. They are removed only when completely independent samples in time are acquired in the high-speed case, thus using a high-speed system as a standard one. Apart from this, the rms fields are in agreement with data in literature as will be shown in the analysis of profiles.

The analysis of combined horizontal and vertical motions is performed on the basis of the non-dimensional Reynolds stress component presented in Fig. 8. The plots from the two PIV systems are very similar and close to the ones reported in the literature on the argument, showing two developing shear layers with opposite signs. The results from the high-speed system are of slightly lower quality in comparison to the standard one although to a lesser extent in comparison to the rms maps shown in Fig. 6. This depends on the different statistical sample size and on the original image quality as acquired by the two cameras and reported in Figs. 2 and 3.

In Figs. 9 and 10, skewness and flatness factors of the axial velocity obtained from the two systems are given; the third and fourth-order moments fields are divided by the appropriate power of rms velocities at each point. The structure of the jet is clearly visible with the developing aperture where skewness values as high as ±2.5 and flatness larger than 15 are observed. At the centreline, the values are close to the Gaussian ones, i.e. 0, skewness, and 3, flatness, with a quite sharp deviation around $x/D \approx 6$. In comparing the two cameras, a larger variability is observed in the high-speed data. This is due to the phenomenon already outlined in rms plots. The vertical bands, especially in the skewness results given in Fig. 9 on the right, are due to differences in the number of effectively independent samples between the two systems. To stress this aspect, only 400 over 10,000 images have been considered for the statistics for the standard system. Thus, in such a condition a set with the same number of uncorrelated samples is obtained allowing a closer comparison between the two systems.

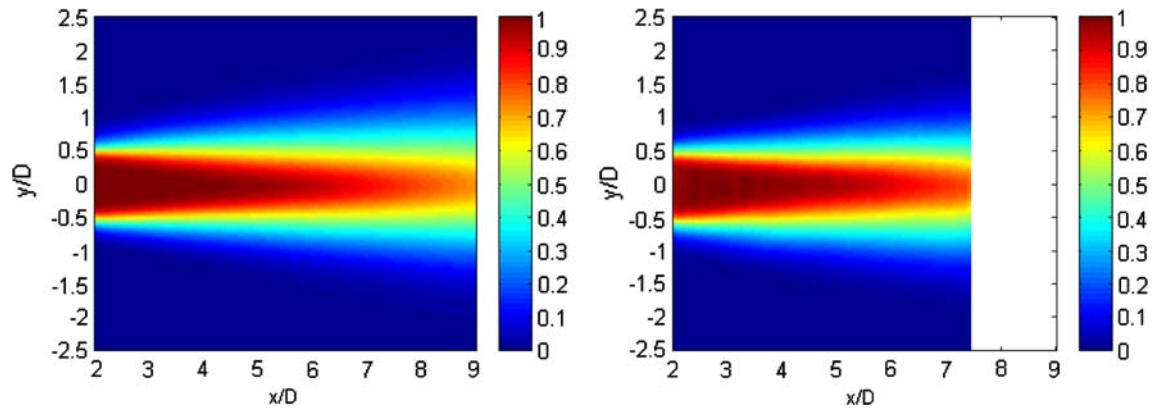

Fig. 6 Average axial velocity, U/U_o for standard (on the *left*) and high-speed (on the *right*) PIV systems in the near jet field

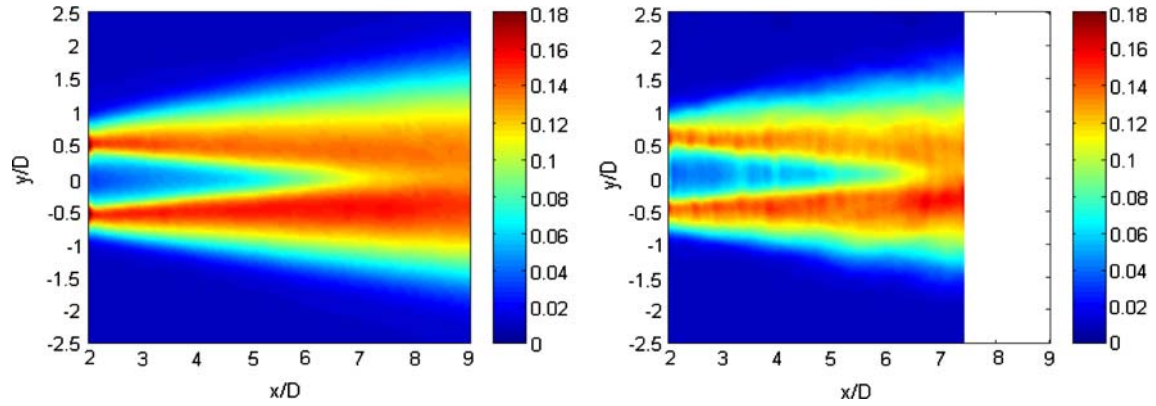

Fig. 7 Rms axial velocity, u'/U_o for standard (on the *left*) and high-speed (on the *right*) PIV systems in the near jet field

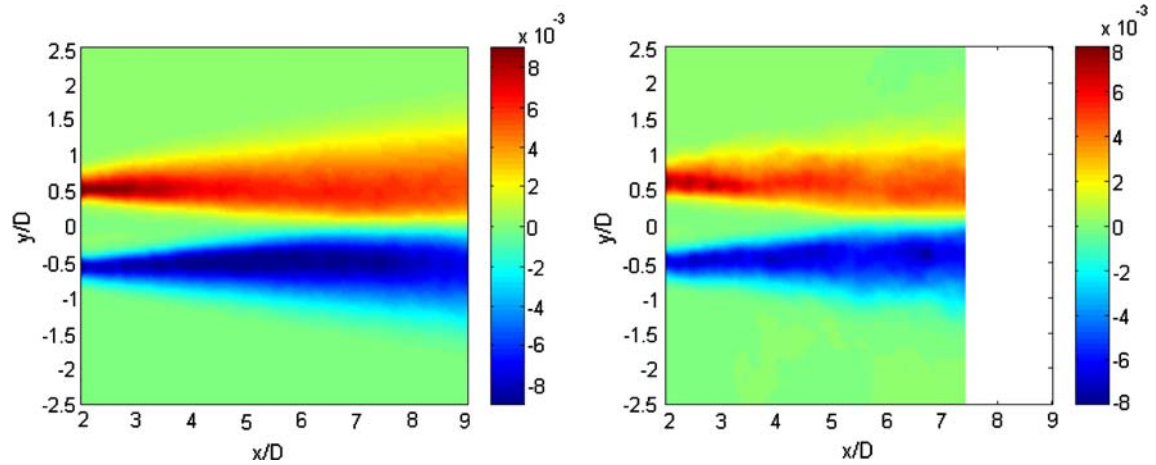

Fig. 8 Reynolds stress component, $u'v'/U_o^2$ for standard (on the *left*) and high-speed (on the *right*) PIV systems in the near jet field

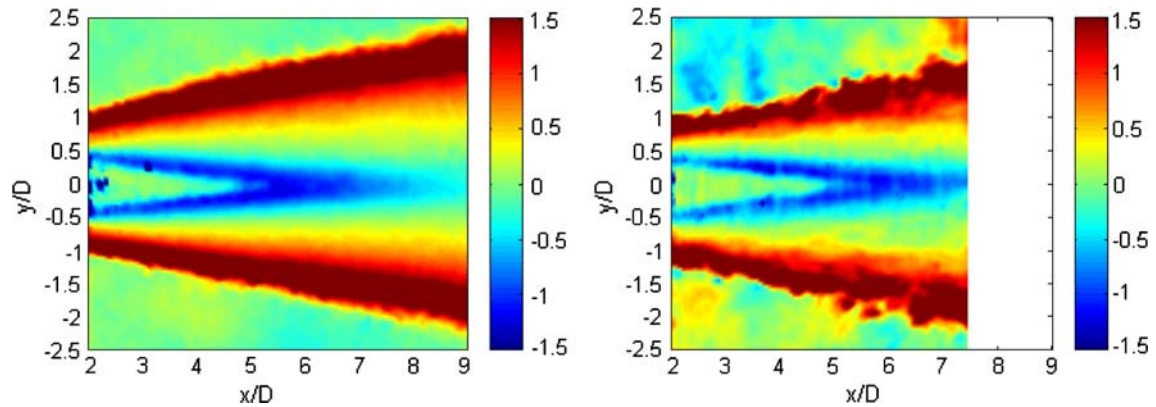

Fig. 9 Skewness factor of axial velocity for standard (on the *left*) and high-speed (on the *right*) PIV systems in the near jet field

In Fig. 11, the results for skewness and flatness for this reduced data set are shown; these plots are very similar to those obtained with the high-speed system reported in Figs. 9 and 10 on the right, i.e. with a similar number of effectively independent samples. Therefore, a careful statistical analysis must be considered to evaluate the frame rate and sample number on the high-order moment statistics, as highlighted by Bendat and Piersol (1971). In any case, differences among data from the two cameras are not larger than 20% up to the fourth-order statistical moment.

A more quantitative comparison is possible based on the profiles of the different quantities along the horizontal and

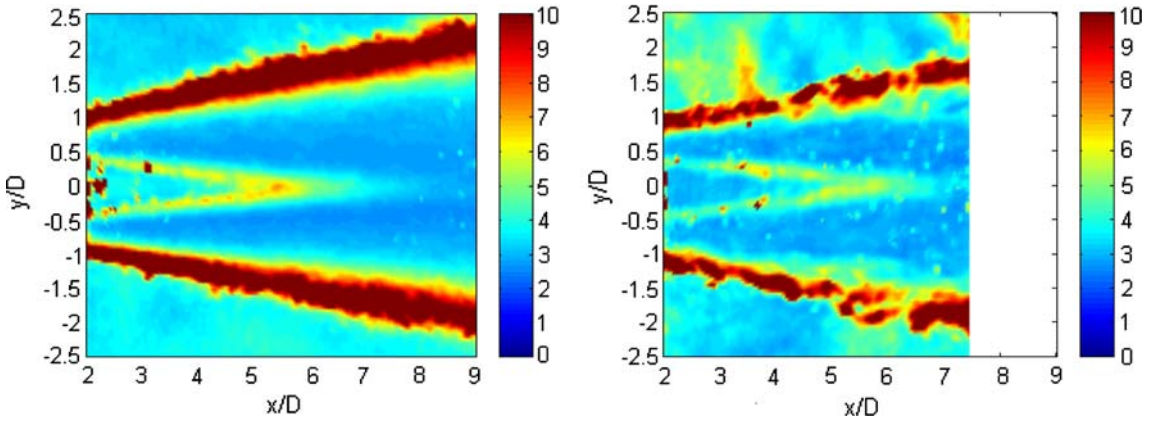

Fig. 10 Flatness factor of axial velocity for standard (on the *left*) and high-speed (on the *right*) PIV systems in the near jet field

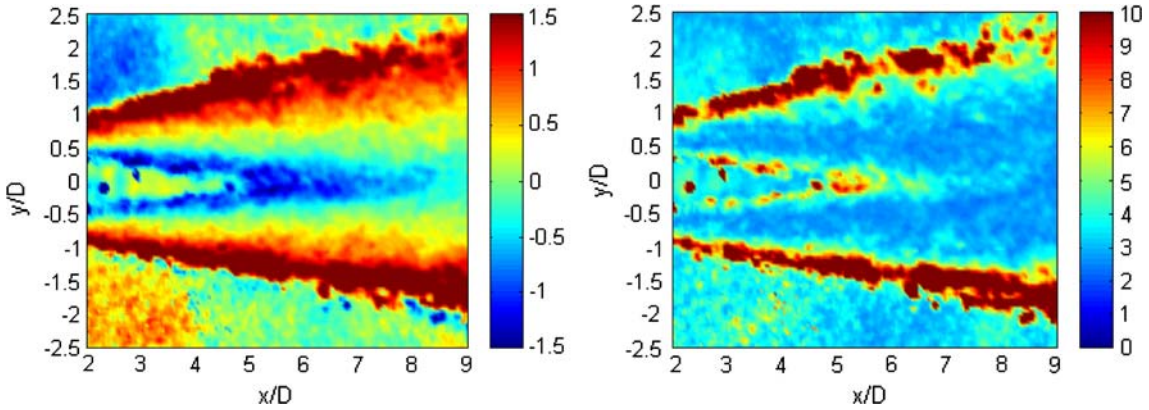

Fig. 11 Skewness (on the *left*) and flatness (on the *right*) factors of axial velocity derived from a standard PIV system using 400 independent images

vertical directions. In Fig. 12, the horizontal profiles, at the centreline, of average axial velocity, axial and vertical rms are shown together with HWA and LDA data previously described in the near, $x/D = 2$–10, and far field, $x/D = 25$–30. The first two graphs correspond to the centreline decay of plots given in Figs. 6 and 7. The continuity between the data close and far from the jet exit is quite good for both systems and for all variables. In particular, the average centreline velocity exhibits the expected $(x/D)^{-1}$ decay as shown by Cohen and Wygnansky (1987) and Liepmann and Gharib (1992). A good agreement with HWA and LDA data, without significant deviations between standard and high-speed systems is achieved too—note that the first plot is in log–log scale. The $(x/D)^{-1}$ velocity centreline decay allows using proper scaling to derive self-similar plots outside the jet core (Hussein et al. 1994; Kuang et al. 2001). These are presented in Fig. 13 for average axial velocity and Reynolds stress at $x/D = 7$. Both systems behave well in comparison to self-similar solution of Eq. 1 and Kuang's law in Eq. 2 for average axial velocity. There is some deviation, about 15%, between the two systems, and from Kuang's law in Eq. 3 too, when considering Reynolds stress. These differences have been already discussed and are due to the different image quality, see Fig. 8. On the other hand, it is important to point out that these curves, which describe the behaviour along the vertical direction, are very smooth and regular. The results from the self-similarity plots confirm the substantial equivalence between the data obtained from cross-correlation and high-speed cameras for low-order velocity moments.

The rms axial profiles, also shown in Fig. 12, provide further insight. The rms increases almost linearly up to the distance where the two shear layers merge, $x/D \sim 6$–7, and then decrease. A difference equal to 15% between the two PIV systems is observed on the rms values of axial velocity, whereas the vertical rms are very close and turbulent intensities as small as 2% are measured. Moreover, in comparing such axial profiles with the vertical ones, reported in Fig. 13, 14, 15 and 16, a lower smoothness for the high-speed data is noticed, especially for the axial component. These aspects confirm that the reasons for the

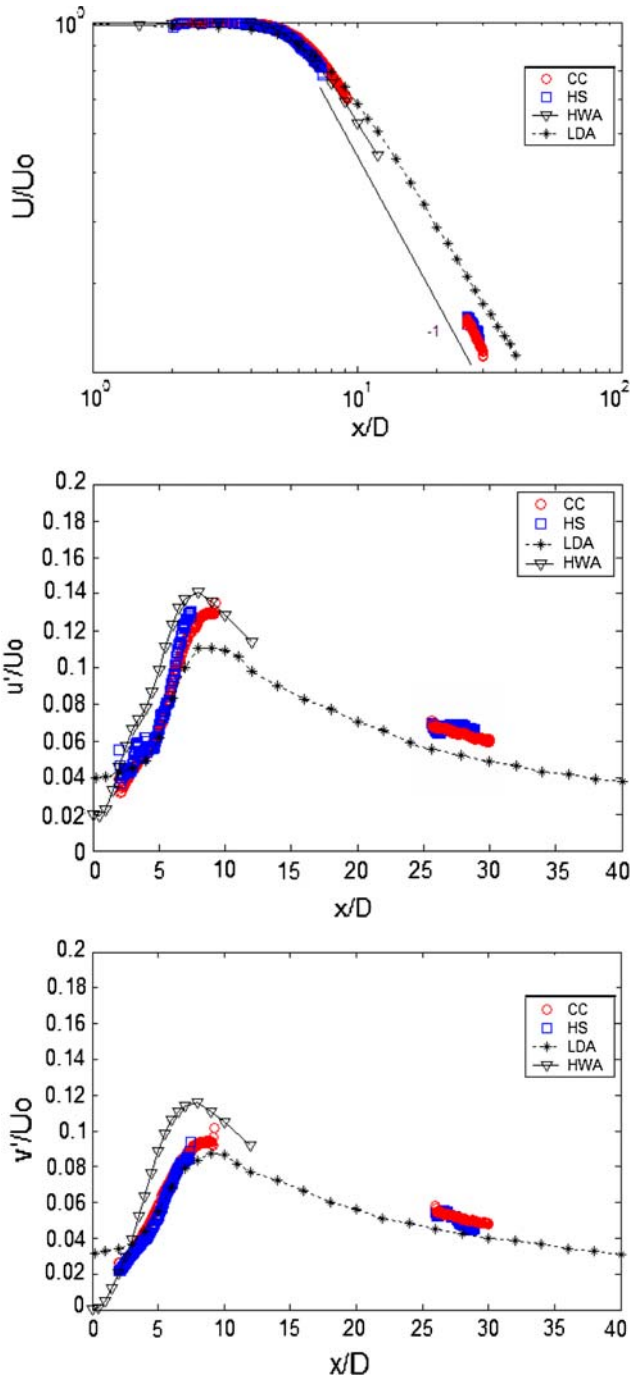

Fig. 12 Average axial velocity, at the *top*, in log scales, rms axial velocity, in the *middle*, and rms vertical velocity, at the *bottom*, axial profiles at the centreline, i.e. at $y/D = 0$, for standard cross-correlation (CC, in *red*) and high-speed (HS, in *blue*) systems in the near and far fields. Comparison with HWA data by Antonia and Burattini (2004) and LDA data by Djeridane et al. (1993)

observed differences are due to the motion along the horizontal which would require a higher statistical ensemble. The present data are generally much closer to the LDA data, obtained almost at the same Reynolds number, than to HWA. So far, in addition to a possible Reynolds number dependence, this disparity is explained also in terms of differences in initial conditions, in particular different initial momentum thickness and turbulence level, between the experiments. As a matter of fact, differences in boundary and initial conditions, as given by the rms values at $x/D = 0$, affect the downstream evolution of the rms field (Hussein et al. 1994 Romano 2002).

These considerations are better outlined in Fig. 14 where radial rms profiles of axial component at $x/D = 2$ and $x/D = 7$ are given. As expected from data in the literature, the rms peak at $y/D = 0.5$ is decreasing and widening when moving downstream. The agreement between results of the two PIV systems is good. Differences are not larger than 15% both at the centreline, $y/D = 0$, and in the shear layers, $y/D = \pm 0.5$, at both axial locations. As already noticed for Fig. 13, these plots along the vertical are much regular and smoother than those along the horizontal, reported in Fig. 7. Also the radial rms profiles at $x/D = 2$ for both PIV systems are closer to the LDA than the HWA at least for $y/D < 0.9$.

Radial rms profiles of vertical component at $x/D = 2$ and $x/D = 7$ are shown in Fig. 15. From the present data, in comparison to the previous axial velocity, the peak at $y/D = 0.5$ is slightly smaller in a closer agreement with LDA. The results from the two camera systems agree between them even better than for rms axial component, even if the disagreement with LDA results is higher than before. In Fig. 16, Reynolds stress $u'v'$ component radial profiles are plotted where only LDA profiles are represented for comparison because HWA data by Antonia and Burattini (2004) were acquired using a single wire. Even in this case the agreement between the two camera systems is remarkable thus confirming the overall satisfactory comparison between the two.

As for the 2D plots presented in Figs. 9 and 10, this comment must be revised when considering axial profiles of third and fourth-order statistical moments. Figure 17 presents the axial profiles of skewness and flatness factors of axial velocity component at the centreline. The values move from a Gaussian trend, $x/D < 4$, to a minimum, for skewness, or maximum, for flatness, and again to Gaussian values (possibly for $x/D > 10$ for skewness factor). The region in which this minimum/maximum is observed is just at the end of the jet core where the two shear layers mix together in the range $x/D \approx 4.5$–7. There are a few differences between skewness and flatness factors obtained with standard cross-correlation and high-speed systems. In particular, both of them present some deviations from LDA data at the lower border of the imaged regions, where PIV algorithm could fail due to border effect (ingoing and outgoing particles). The PIV skewness from both PIV data for $x/D < 5$ also deviate from the LDA, reflecting differences in the turbulence

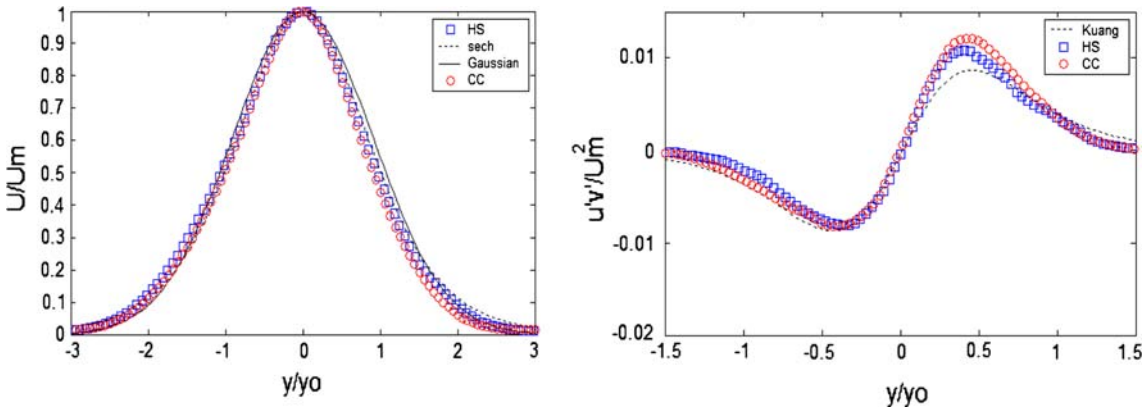

Fig. 13 Average axial velocity, on the *left*, and Reynolds stress, on the *right*, radial profiles for standard cross-correlation, in *red*, and high-speed, in *blue*, systems at $x/D = 7$. Comparison with Eq. 1, 2 and 3 by Hussein et al. (1994), Kuang et al. (2001)

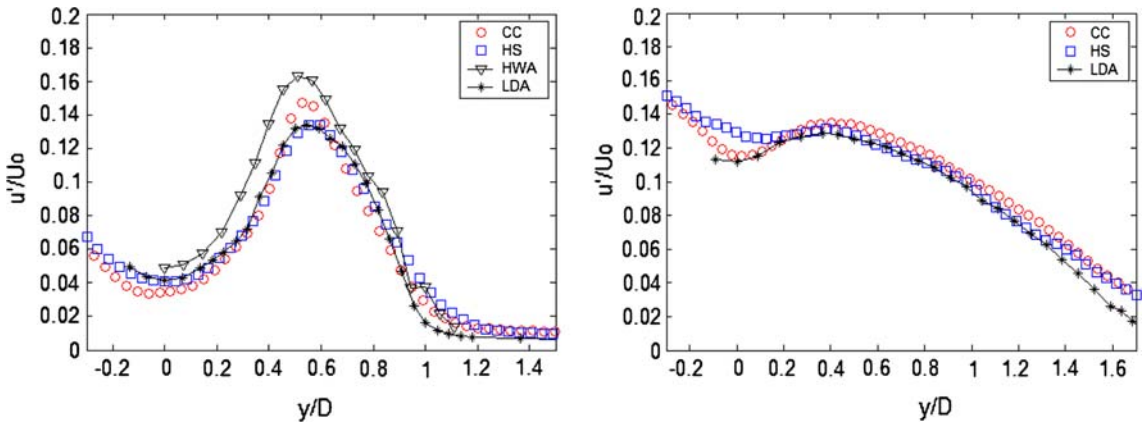

Fig. 14 Rms axial velocity radial profiles for standard cross-correlation, in *red*, and high-speed, in *blue*, systems at $x/D = 2$, on the *left*, and $x/D = 7$, on the *right*. Comparison with HWA data by Antonia and Burattini (2004) and LDA data by Djeridane et al. (1993)

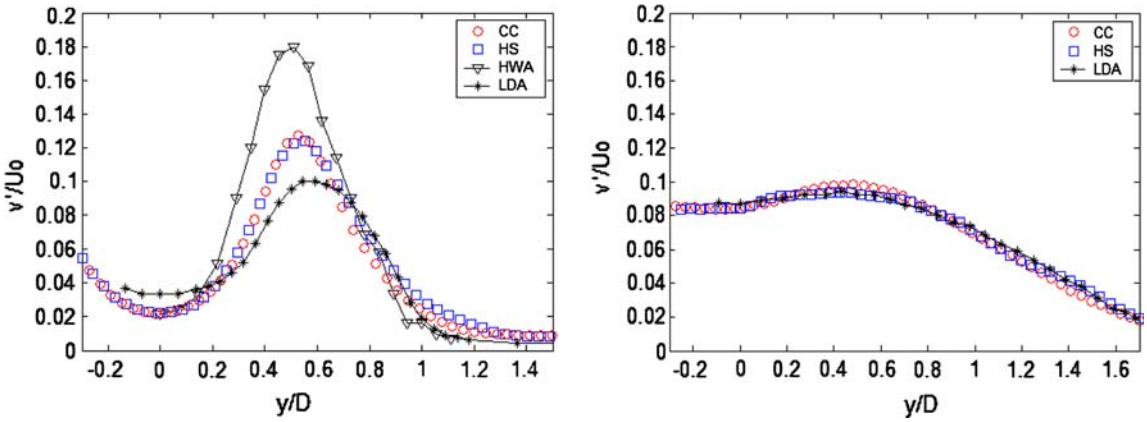

Fig. 15 Rms vertical velocity radial profiles for standard cross-correlation, in *red*, and high-speed, in *blue*, systems at $x/D = 2$, on the *left*, and $x/D = 7$, on the *right*. Comparison with HWA data by Antonia and Burattini (2004) and LDA data by Djeridane et al. (1993)

level at the jet exit due to different initial conditions between the two experiments. In addition, data from high-speed camera show a poorer statistical convergence in the form of oscillations around the average behaviour on both moments, especially when they deviate from the Gaussian values, but generally on all skewness data. In agreement with results from Figs. 9 and 10, this seems to be a relevant drawback when using a PIV system based on high-speed cameras. The investigation of the velocity derivative field, especially important when measuring

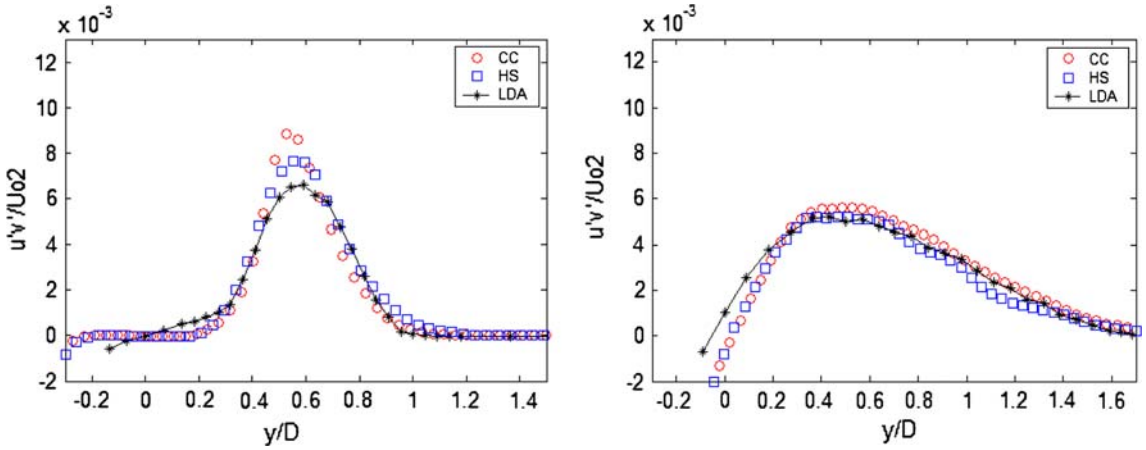

Fig. 16 Reynolds stress radial profiles for standard cross-correlation, in *red* and high-speed, in *blue*, systems at $x/D = 2$, on the *left*, and $x/D = 4$, on the *right*. Comparison with LDA data by Djeridane et al. (1993)

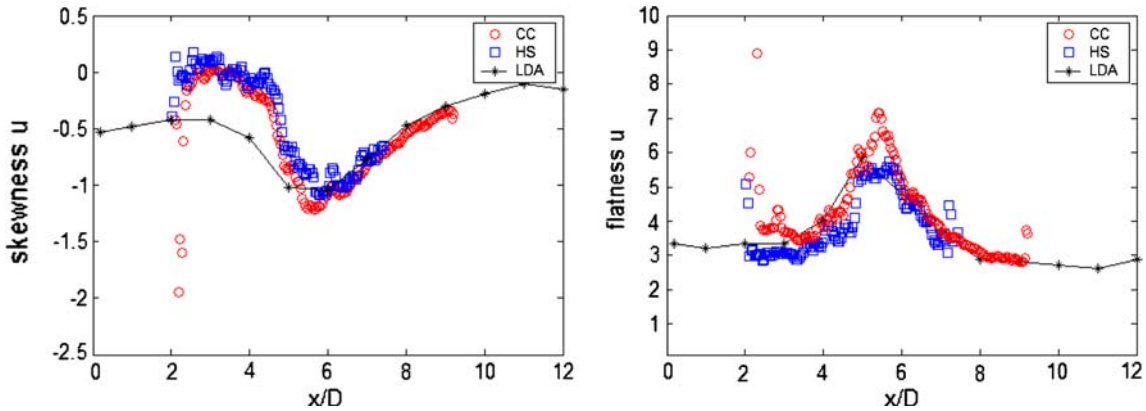

Fig. 17 Centreline axial profiles of skewness, on the *left*, and flatness, on the *right*, factors of axial velocity for standard cross-correlation, in *red*, and high-speed, in *blue*, systems in the near field. Comparison with LDA data by Djeridane et al. (1993)

turbulent kinetic energy dissipation, helps in investigating this point.

5.2 Statistics of velocity derivatives

The computation of derivatives from experimental data is a quite severe test to point out the presence of noise and/or disturbances (Saarenrinne and Piirto 2000). Velocity derivatives have been evaluated by using a central difference scheme and the used 75% overlapping between PIV interrogation windows is just a compromise between resolution, numerical estimation and time consuming requirements. In Fig. 18, the profile of mean square axial derivative of axial velocity, based on the fluctuating velocity component, is shown. Specifically,

$$\varepsilon_{\text{iso}} = 15\nu\overline{\left(\frac{\partial u}{\partial x}\right)^2} \tag{4}$$

i.e. the isotropic form of the turbulent kinetic energy (TKE) dissipation rate, has been plotted, where ν is the kinematic viscosity and the overbar denotes averaging in time. As usual, ε_{iso} is non-dimensional by D and U^3 (Monin and Yaglom 1975). As for the velocity field, also in mean square derivatives, disturbances, in the form of oscillations, appear in the data from the high-speed PIV systems. They are emphasised in comparison to those already observed in axial rms velocity plots, Fig. 12, since derivatives enhance data gradients. The plots point out the spatial evolution of the small-scale field, which dominates the kinetic energy dissipation and is usually not easily discernible from experimental noise. It is expected that this quantity would increase in the near-outlet region as a consequence of the increased production of TKE (Hussein et al. 1994). For the present results, the data from the standard camera system are sufficiently clear and smooth to depict a range, between $x/D = 3.5$–6.5, with an increase of the TKE dissipation as the fourth-power of the axial distance. The best power-law order and the range have been determined by dividing the quantity by the power-law itself. This increase is in agreement with the observed increase of the rms axial

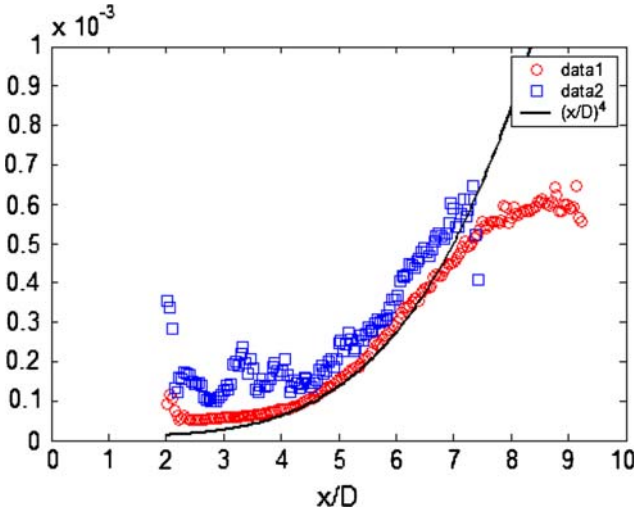

Fig. 18 Centreline axial profiles of turbulent kinetic energy dissipation rate, $\varepsilon_{iso}\, D/U^3$ for standard cross-correlation, in *red*, and high-speed, in *blue*, systems in the near field. The axial distance fourth-power law is also shown

velocity given in Fig. 12 (almost as the third-power of the axial distance). Even the data from the high-speed system reveal this behaviour although partially hidden by the disturbances along the axis.

It would be interesting to consider if similar conclusions can be derived from mean square derivatives along the other directions, using also the other measured velocity components. In Fig. 19, the other four measured in-plane derivatives are presented using the same dimensionless variables as in Fig. 18, included the cross term.

All terms have more or less the same order of magnitude except for the cross-term which is about (1/3–1/8) of the others. The mean square derivative of the axial component along the radial, y, direction is the largest one, top-left part of Fig. 19. The data from the two PIV systems agree quite well even if, as for the previous mean square derivative, Fig. 18, the data from the high-speed system show some oscillations. Considering that these oscillations are much lower on derivatives of vertical velocity, and of the cross-term too, as presented in the other parts of Fig. 19, it is possible to state that the present data derived from a high-speed system show an axial velocity component much more affected from image noise and statistical ensemble features than the vertical. This statement on the derivative field is in agreement with results obtained for the velocity field in previous subsection (Figs. 12, 14, 15, 16). In each part of Fig. 19, the best power-law fit has been determined, as for data presented in Fig. 18. Except for the mean square derivative of the axial component along the radial direction, reported in the top-left part of Fig. 19, which exhibits a clear power-law only on a reduced interval, all derivatives indicate an increase as third or fourth-power of the distance. Roughly, the third-power seems to be more suitable for derivatives along the vertical, while the fourth-power is better suited for those along the horizontal and for the cross-term. This seems to be a very relevant result for implementing numerical computations and it is important to consider that it can be recovered both from the standard cross-correlation and from the high-speed PIV system.

To account for recovery of isotropy when moving downstream, the previous mean square derivatives have been used to derive the following derivative ratios which are reported in Fig. 20

$$K_1 = \frac{\overline{(\partial v/\partial x)^2}}{\overline{\left(\partial u/\partial x\right)^2}}, \quad K_2 = \frac{\overline{(\partial u/\partial y)^2}}{\overline{\left(\partial u/\partial x\right)^2}},$$
$$K_3 = \frac{\overline{(\partial v/\partial y)^2}}{\overline{\left(\partial u/\partial x\right)^2}}, \quad K_4 = \frac{\overline{(\partial u/\partial y)(\partial v/\partial x)}}{\overline{\left(\partial u/\partial x\right)^2}} \tag{5}$$

The isotropic values for these ratios are $K_1 = 2$, $K_2 = 2$, $K_3 = 1$, $-K_4 = 0.5$, see Monin and Yaglom (1975). Close to the jet exit the derivative ratios increase up to a maximum at the end of the core region, approximately $x/D = 5$, and then approach the far field values with slight increase for K_1, K_3, K_4 and decrease for K_2. It seems that, except for K_1, the values attained from the two PIV systems at $x/D = 7$ ($K_1 = 0.8$–1.2, $K_2 = 2.0$–2.4, $K_3 = 0.8$ and $-K_4 = 0.25$–0.30) are close to isotropy even at this near field location. Values obtained from the present experiment in the far field, at $x/D = 30$, are $K_1 = 1.6$, $K_2 = 1.8$, $K_3 = 1$ and $-K_4 = 0.4$, indicated by thick bars in Fig. 20. This fact points out that the first ratio, K_1, and partially the cross-term, are the ones more affected by the anisotropic conditions at the jet outlet and only slightly approach isotropy if the far field values are considered. This statement is confirmed by measurements of other authors summarised by George and Hussein (1991).

For comparison, it is important to note that in locally axisymmetric homogeneous turbulence the theoretical values are $K_3 = 0.3$ and $K_4 = -0.5$, as stated by George and Hussein (1991), while experimental values in the far field are $K_1 = 1.3$ and $K_2 = 1.7$, see Hussein (1994).

In addition to a larger variability of the high-speed camera the two cameras do not give information of similar quality. Indeed, it is important to notice that, except for K_2, the data from the high-speed system are always biased towards smaller values than those by the standard one. By considering again Fig. 18, it is possible to observe that the mean square derivative in relation Eq. 4 is always overestimated by the high-speed system in comparison to the standard system of at least by 20%. Thus, derivative ratios in (5) are expected to be underestimated, except for the ratio K_2 in which also the other term is slightly overestimated, see Fig. 19, top-left.

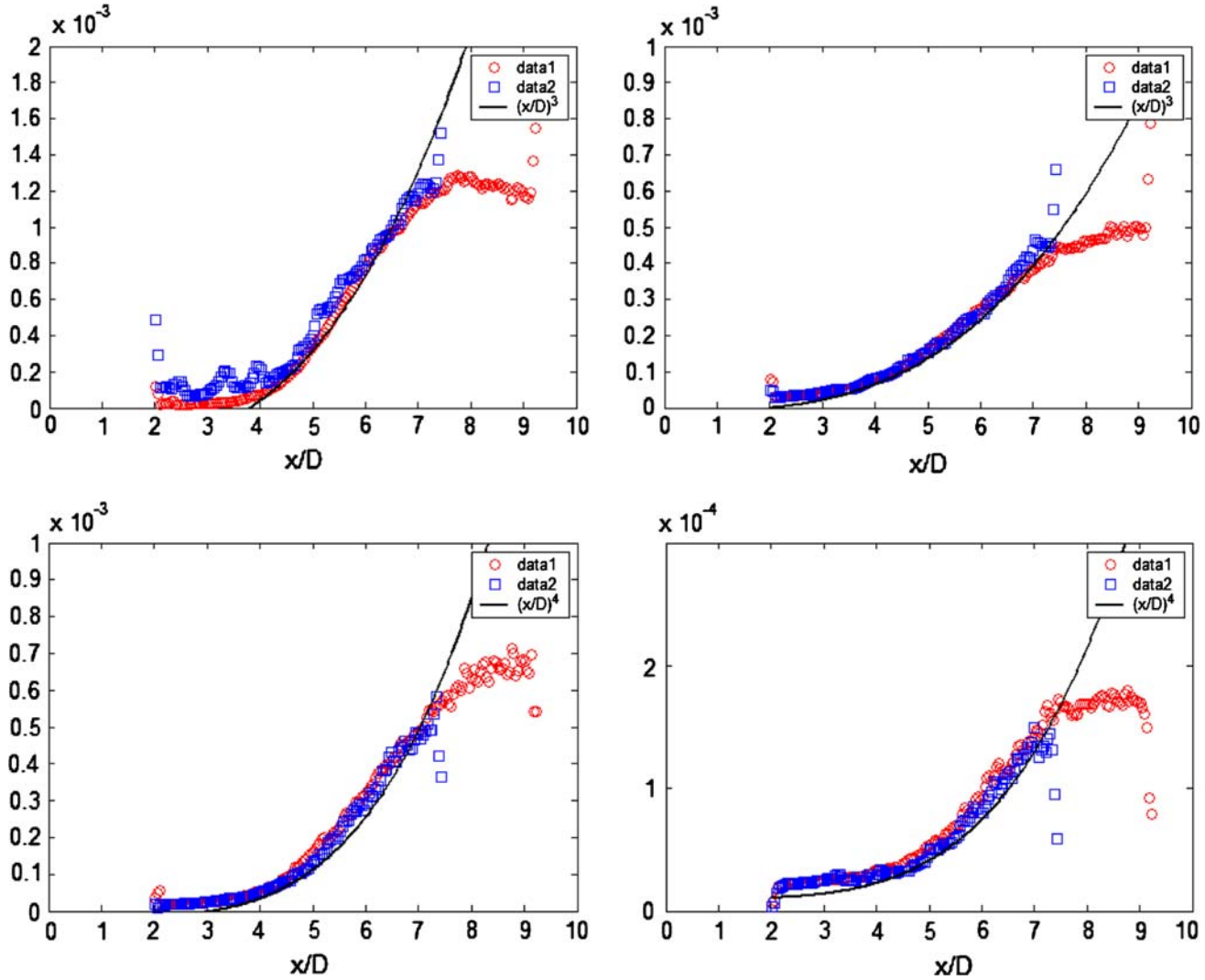

Fig. 19 Centreline axial profiles of mean square velocity derivatives non-dimensional by U^3/D: $\overline{\left(\partial u/\partial y\right)^2}$ at the *top* on the *left*, $\overline{\left(\partial v/\partial y\right)^2}$ at the *top* on the *right*, $\overline{\left(\partial v/\partial x\right)^2}$ at the *bottom* on the *left* and $-\overline{\left(\partial u/\partial y \partial v/\partial x\right)}$ at the *bottom* on the right. Data are in the near field, standard cross-correlation system, *red*, and high-speed one, HS, *blue*. The power-law fits are also shown

The overestimated terms are just those in which mean square derivatives of axial velocity component are considered, reflecting the enhanced influence of noise and disturbances for horizontal displacements. In any case, the derivative ratios are even more sensitive to data quality than the mean square derivative themselves which are in reasonable agreement between the two systems, Fig. 19, and give a limit on the quality of statistical data derived from the present high-speed system.

6 Conclusions

In this paper, the well documented circular turbulent jet flow is under investigation to compare the velocity fields from images acquired by standard cross-correlation and high-speed particle image velocimetry (PIV) systems. Both these are commonly used in PIV, so questions arise on the effects of the different sensor configuration (CCD for cross-correlation and CMOS for high speed), of related noise levels and image acquisition procedures on obtaining statistical quantities. In particular, it is interesting to point out the effects on the flow small-scale evaluation, on the order of the Taylor and Kolmogorov microscales, which dominate the higher order velocity moments and velocity derivatives whose correct evaluation is important for the determination of the turbulent kinetic energy dissipation frequently used in flow modelling by numerical codes.

It is important to remark that the two cameras employ different image acquisition modes. For standard cross-

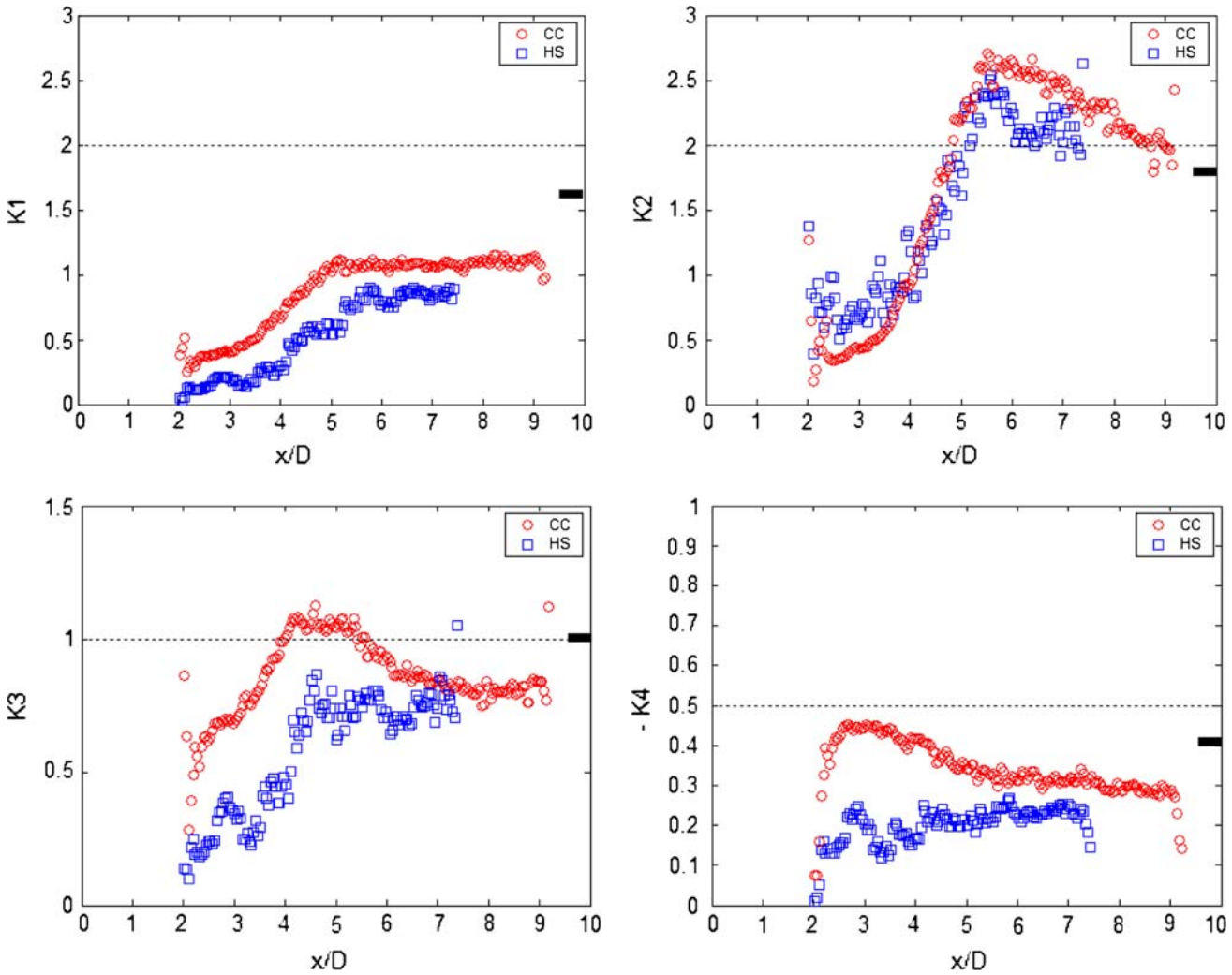

Fig. 20 Centreline axial profiles of ratios K_1 at the top on the *left*, K_2 at the top on the *right*, K_3 at the bottom on the *left* and $-K_4$ at the bottom on the *right*, defined in Eq. 5 for standard cross-correlation, in *red*, and high-speed, in *blue*, systems in the near field. The small horizontal thick bars indicate the far field values, measured at $x/D = 30$, while the horizontal dotted lines the isotropic values ($K_1 = 2$, $K_2 = 2$, $K_3 = 1$, $-K_4 = 0.5$, respectively)

correlation, an image pair is acquired in a very short time interval, less than the flow temporal microscales, and the successive pair is acquired after about one integral time scale—i.e. the second pair is completely independent on the first and so on. On the other hand, for a high-speed camera, a sequence of images, usually thousands, with small time interval, on the order of flow microscale, is acquired continuously for a time interval not longer than an integral time scale. Thus, for a PIV system based on a high-speed camera, the image pairs used for PIV analysis are not effectively independent. As a matter of fact, a high-speed camera is commonly employed to investigate the time flow evolution and consequently image pairs must have a time relation between them. Nonetheless, the question of deriving single-point statistical properties is still open due to the fact that these are always derived from such a high-speed camera PIV system working in high frame-rate mode. Special procedures, for example by dividing the acquisition interval in subsets, can be employed to improve the statistics ensemble as in the present investigation. In any case, the effective number of independent data is not equal to the number of image pairs acquired so that this difference in comparison to standard PIV system must be considered.

Another point to be considered is the different sensor configuration, CCD or CMOS, which gives a quite different image quality. As documented in this paper, the different behaviour of the low intensity level pixels and the effect on the small scale motion could be relevant. It is very important to notice that recent CMOS cameras, when the illumination levels are not too low and no image intensifier is used, are able to attain almost the same signal to noise

ratio (SNR) and spatial uniformity as CCD based cameras. In this sense, being the optimal illumination level strictly related to the camera used, the high-speed camera plus illumination equipment must be considered as a whole so that it is correct to speak about high-speed PIV systems rather than high-speed PIV camera alone.

The results from the present comparison of performances show that the average velocity field is well determined with both types of PIV systems. Even the velocity probability density distributions appear similar. Slight differences appear in the form of disturbances along more or less vertical bands in the second-order velocity statistics especially of the axial velocity. They are related to the procedure used to acquire images: the ensemble is subdivided in 200 subsets of 50 images each one so that there are 49 strongly inter-related velocity fields separated from the other equivalent subset by a time interval as long as the flow integral time scale. Thus, the whole sequence appear as the sum of many discrete image subsets each one consisting of 49 fields covering, when moving more or less along the jet axis, about one jet diameter. Thus, especially the measured axial velocity results suffer from these more or less vertical discontinuities in higher-order statistics: as a consequence, the results show disturbances in the form of vertical bands which do not allow to smoothly describe the entire flow field. A possible solution would be to use subsets each one composed of only one image pair, but this of course is just the operating condition of standard cross-correlation camera and not that of a high-speed one. The use of subsets retains both the advantages of acquiring correlated and uncorrelated samples depending on the quantities to be determined. The present data confirm that this acquisition mode used with a high-speed PIV system is able to give horizontal and vertical profiles of mean and rms velocities in good agreement not only with those obtained from a standard cross-correlation camera system but also with those from other measurement techniques. In any case, the previous statistical limitations on high-speed system are more evident when considering third- and fourth-order velocity moments.

The situation changes when considering statistics of velocity derivatives. The subset acquisition used with the high-speed system, although revealing the basics, does not allow attaining the same quality of results as that from a standard PIV system. In particular, mean square derivative statistics, which is the base for obtaining the turbulent kinetic energy dissipation, of high-speed system is quite affected by disturbances (in this case also an important contribution from the acquired image noise from CMOS sensors cannot be ruled out). As for the velocity fields, also for derivatives, the axial velocity is much highly influenced. This is particularly critical when considering that several isotropy relations and indicators use the mean square derivative of axial velocity component as a basis.

In summary, it was a common practice in HWA and LDA past investigations to perform data acquisition at relatively low data rate for long time intervals, in comparison to the flow integral scales, when computing single-point statistics. On the other hand, the highest possible data rate for relatively short time intervals was requested for multi-point statistics related to correlation and spectral functions. The results of the present study involving cross-correlation and high-speed PIV systems confirm that this practice is still valid even for PIV data. The present data also show that for all tested quantities, velocity and derivative statistics, the results obtained with the two systems are substantially equivalent, providing that the statistical ensemble is built up properly. Thus, the present investigation confirms that advanced high-speed CMOS cameras used in PIV must be used with a certain care and that an evaluation of flow time scales is always a preliminary requirement before performing flow measurements.

Acknowledgments The authors gratefully thank Dr. Francisco J.A. Pereira for many helpful comments and suggestions.

References

Antonia RA, Burattini P (2004) Small-scale turbulence: how universal is it? In: Proceedings of 15th Australasian fluid mechanics conference. Sydney, Australia

Bendat JS, Piersol AC (1971) Random data: analysis and measurement procedures. Wiley, London

Brucker C (1997) 3-D scanning PIV applied to an air flow in a motored engine using digital high-speed video. Meas Sci Technol 8:1480–1492

Burattini P, Antonia RA, Danaila L (2005) Similarity in the far field of turbulent round jet. Phys Fluids 17:025101

Burgmann S, Brücker C, Schröder W (2006) Scanning PIV measurements of a laminar separation bubble. Exp Fluids 41:319–326

Cohen J, Wygnansky I (1987) The evolution of instabilities in the axisymmetric jet. Part 1. The linear growth of disturbances near the nozzle. J Fluid Mech 176(19):1–219

Djeridane T, Amielh M, Anselmet F, Fulachier L (1993), Experimental investigation of the near-field region of variable density turbulent jets. In: Proceedings 5th international symposium on refined flow modeling and turbulence measurement. Paris, France. web: http://cfd.me.umist.ac.uk/ercoftac/classif.html

Etoh TG, Takehara K, Takano Y (2001) High-speed image capturing for PIV. In: Proceedings 4th international symposium on particle image velocimetry. Gottingen, Germany

George WK, Hussein JH (1991) Locally axisymmetric turbulence. J Fluid Mech 233:1–23

Hain R, Kahler CJ (2005), Advanced evaluation of time-resolved PIV image sequences, In: Proceedings 6th international symposium on particle image velocimetry. Pasadena, USA

Hain R, Kahler CJ, Tropea C (2007) Comparison of CCD, CMOS and intensified cameras. Exp Fluids 42:403–411

Hinze JO (1975) Turbulence. McGraw-Hill, New York

Hussein JH (1994) Evidence of local axisymmetry in the small scales of a turbulent planar jet. Phys Fluids 6(6):2058–2070

Hussein JH, Capp SP, George WK (1994) Velocity measurements in a high-Reynolds-number, momentum-conserving, axisymmetric, turbulent jet. J Fluid Mech 258:31–75

Kuang J, Hsu CT, Qiu H (2001) Experiments on vertical turbulent plane jets in water of finite depth. J Eng Mech 1:18–26

Lecordier B, Trinité M (1999), Time-resolved PIV measurements for high-speed flows. In: Proceedings 3rd international workshop on particle image velocimetry. Santa Barbara, USA

Liepmann D, Gharib M (1992) The role of streamwise vorticity in the near-field entrainment of round jets. J Fluid Mech 245:643–668

Monin A, Yaglom AM (1975) Statistical fluid mechanics: mechanics of turbulence. MIT Press, Cambridge

Raffel M, Kompenhans J, Stasicki B, Bretthauer B, Meier GEA (1995) Velocity measurement of compressible air flows utilizing a high-speed video camera. Exp Fluids 18:204–206

Romano GP (1998) Investigation on particle trajectories and Lagrangian statistics at the outlet of a circular jet. Exp Therm Fluid Sci 17:116–123

Romano GP (2002) The effect of boundary conditions by the side of the nozzle of a low Reynolds number jet. Exp Fluids 33:323–333

Saarenrinne P, Piirto M (2000) Turbulent kinetic energy dissipation rate estimation from PIV velocity vector fields. Exp Fluids 29(7):S300–S307

Scarano F (2003) Theory of non-isotropic spatial resolution in PIV. Exp Fluids 35:268–277

Stanislas M, Okamoto K, Kahler CJ, Westerweel J, Scarano F (2008) Main results of the third International PIV Challenge. Exp Fluids 45:27–71

Tennekes H, Lumley JL (1970) A first course in turbulence. MIT Press, Cambridge

Towers DP, Towers CE (2004) Cyclic variability measurements of in-cylinder engine flows using high-speed particle image velocimetry. Meas Sci Technol 15:1917–1925

Triep M, Brücker C, Schröder W (2005) High-speed PIV measurements of the flow downstream of a dynamic mechanical model of the human vocal folds. Exp Fluids 39:232–245

Westerweel J, Dabiri D, Gharib M (1997) The effect of a discrete window offset on the accuracy of cross-correlation analysis of digital PIV recordings. Exp Fluids 23:20–28

Williams TC, Hargrave GK, Halliwell NA (2003) The development of high-speed particle image velocimetry (20 kHz) for large eddy simulation code refinement in bluff body flows. Exp Fluids 35:85–91